AIAA 81-0999BR

Damped Euler-Equation Method to Compute Transonic Flow Around Wing-Body Combinations

Arthur Rizzi*
FFA The Aeronautical Research Institute of Sweden, Bromma, Sweden

Inviscid transonic flows containing either strong shock waves or complex vortex structure call for the Euler equations as a realistic model. Presented here is a computational procedure for solving the Euler equations for transonic flow around a wing and fuselage upon an O-O mesh generated by transfinite interpolation. An explicit time-marching finite-volume procedure solves the flow equations and features a nonreflecting far field boundary condition, an internal mechanism for temporal damping, and use of the local time step, all of which improve the convergence of the computation. Converged after several hundred iterations, results computed on the CYBER 203 vector processor are compared with experimental data and potential-flow computations. The Euler-equation model is found to predict the existence of a tip vortex created by inviscid flow separation in the downstream region of the tip of the M6 wing where the radius of curvature approaches zero.

Introduction

LAST year a workshop[1] was held in order to assess the currently used computational procedures, one against the other, in several carefully specified two-dimensional transonic flow problems. While reasonable agreement among the results given by the various full potential and Euler-equation methods was obtained in the subcritical cases, a disparity between the results of these two models was found to grow with cases of increasing shock strength. For the NACA 0012 airfoil and conditions $M=0.80$ and $\alpha=1.25$ deg, for example, the lift coefficients C_L given by all the Euler methods ranged between 0.30 and 0.38, whereas the range of C_L for the potential method was 0.28-1.1. This discrepancy has led to a reconsideration of the validity of the potential model when strong shocks are present in the flow, not only locally in terms of the isentropic shock jumps but also, and perhaps even more importantly, with regard to the correct modeling of vortex phenomena throughout the entire flowfield. In the potential representation the vorticity that is bound to the airfoil is accounted for by a jump in the potential across a line originating at the trailing edge and lying a priori along some chosen coordinate direction downstream, the so-called Kutta condition. The Euler equations, in contrast, admit vorticity in the solution and the equivalent to the Kutta condition evidently does not need to be enforced explicitly. This situation is currently under study by researchers using a variety of numerical methods. In three dimensions the flow past a finite wing is even more complex and less is known. Vortices, for example, are shed continuously from the wing tips and the entire trailing edge. Whether a Kutta condition or its equivalent is necessary in this case has not been investigated, but because vorticity is so crucial to the realism achieved by inviscid flow models, interest has been aroused in questions like this and in numerical methods that solve the Euler equations. A number of methods[2-4] exist to solve the Euler equations for three-dimensional flow, but they have been developed exclusively for and applied only to internal flows. Apparently, the solution of the Euler equations for external flow past a finite wing with lift has not been given before.[5]

The construction itself of a coordinate mesh around even a simple wing-body configuration is not a trivial matter, and the numerical solution of the Euler equations upon it is indeed a formidable computational task, which in turn puts a high premium on a mesh generator that can provide an optimum resolution with an economy of nodal points. The present view is that these two items, mesh construction and solution procedure, are separate and distinct operations, and as such should be treated in an independent and modular way, i.e., the means for generating a mesh should not be dictated by the limitations of a given specific flow-solution procedure and, conversely, the method that determines the flow should accept as input an arbitrary set of coordinate points which constitutes the mesh. In practice, of course, these two operations can never be totally independent because the logistic structure of the data, the location of outer boundaries, the nature of coordinate cuts, and the types of mesh singularities are items that have to be closely coordinated between the flow solver and the mesh generator. Based on a rather advanced mapping, designated O-O, the grids used here are constructed by Eriksson's generalized transfinite interpolation method which is described, and the grids are displayed, in the companion paper.[6] The O-O mesh is attractive because for a given number of points it offers a near maximum resolution at both the leading and trailing edges as well as at the tip of the wing and because it possesses only regular singularities.

Featuring the first use of the O-O mesh, this paper presents a pseudo-unsteady explicit finite-volume procedure to solve the Euler equations that introduces an internal temporally dissipative damping mechanism and marches the solution forward with the local time step. Nonreflecting far-field boundary conditions of the type of Enquist's first approximation are used with the modification that an energy-absorbing mechanism is added in order to damp reflections from the nonperfectly absorbing boundaries. Results for the ONERA M6 wing and the RAE A/B_2 wing-body combination in transonic flow have been computed in several hundred instead of several thousand iterations and are compared with experimental data and the computations of a potential method. One conclusion is that the Euler equation realistically represents the rotational nature of the flow including the vortex shed from the tip of the M6 wing even without the explicit use of a Kutta condition. We attribute this phenomenon of inviscid flow separation to a mechanism intrinsic to the Euler equations.

Presented as part of Paper 81-0999 at the AIAA 5th Computational Fluid Dynamics Conference, Palo Alto, Calif., June 22-23, 1981; submitted Jan. 4, 1982. Copyright © 1982 by Arthur Rizzi. Published by the American Institute of Aeronautics and Astronautics with permission.

*Research Scientist, Aerodynamics Department. Member AIAA.

Numerical Solution Procedure

Our method to solve the flowfield is the false transient or pseudo-unsteady approach that marches a hyperbolic system of equations forward in time, without strict concern for time accuracy, until a steady state is reached. The convergence of this formulation is generally slow, and Viviand's analysis[7] of the asymptotic large-time behavior of the unsteady approach provides some understanding of why many time iterations are required. He points out that although transients in the solution to the differential equations are neither damped nor amplified, a steady state can be achieved if these transients are damped by the difference scheme and if they are passed out of the bounded computational domain by the boundary conditions. Nonreflecting boundary conditions and a temporally damped time integration scheme are two features of this method specifically designed to improve the convergence of the computation.

Continuum Equations

The (Euler) equations of motion in integral form are

$$\frac{\partial}{\partial t}\int_{\Omega} q\,\mathrm{dvol} + \int\int_{\partial\Omega} \boldsymbol{H}\cdot\boldsymbol{n}\,\mathrm{d}s = 0 \tag{1}$$

where $q=[\rho,\ \rho u,\ \rho v,\ \rho w]$ is the density and rectangular components of momentum referred to a Cartesian system x,y,z fixed in space. The quantity $\boldsymbol{H}(q)=[q\boldsymbol{V} + (0,\boldsymbol{e}_x,\boldsymbol{e}_y,\boldsymbol{e}_z)p]$ represents the net flux of q transported across, plus the pressure p acting on, the closed surface $\partial\Omega$ that bounds the volume Ω with unit normal $\boldsymbol{n}$. We only treat flows with a globally constant stagnation enthalpy h_0 so that for a perfect gas the Bernoulli equation $p=\frac{1}{2}\kappa\rho(2h_0-u^2-v^2-w^2)$ where $\kappa=\gamma/\gamma-1$ completes system (1).

Dividing by Ω and then shrinking Ω to a point leads to the differential conservation law valid at that point if the partial derivatives are continuous there. Conceptually, however, we find it more appealing to difference the finite-domain integral system (1) directly, the so-called finite-volume approach,[8] since the integral law formally does not exclude discontinuities from the interior of Ω. Our method, therefore, is a cell concept rather than a grid-point concept. The integral approach may be important for the correct capturing of discontinuities in the flow. It also lends itself to an obvious geometrical interpretation between the dependent and independent variables in the physical space and their counterparts in the computational space which makes the use of any arbitrary coordinate system more readily comprehensible.

Finite-Volume Discretization

A grid of cells packed so that they discretize the flowfield is constructed by the transfinite grid-generation technique described in Ref. 6. Founded on the generating parameters I, J, K, the edges of the cells define the nonorthogonal coordinate directions X_I, X_J, X_K in physical units and the unit vectors $\boldsymbol{n}_I$, $\boldsymbol{n}_J$, $\boldsymbol{n}_K$ are normal, respectively, to the grid surfaces I, J, K equal to constants. Since Eq. (1) is valid for any arbitrary volume it also holds locally for each individual cell i, j, k in the mesh where the bounding surface $\partial\Omega_{ijk}$ now consists of the family of the three coordinate surfaces $\boldsymbol{S}=\{\boldsymbol{S}_I,\boldsymbol{S}_J,\boldsymbol{S}_K\}$ that delineate the hexahedronal mesh cell (Fig. 1).

In order to solve this continuum equation we must evaluate the integrals by some discrete approximation which then characterizes the class of the cell method. Here we consider only a single-point evaluation per cell for the dependent variables q so that by the mean value theorem Eq. (1) becomes

$$\Omega_{ijk}\frac{\partial q_{ijk}}{\partial t} + \delta[\boldsymbol{H}(q)\cdot\boldsymbol{S}]_{ijk} = 0 \tag{2}$$

where q_{ijk} is now interpreted as a volumetric average located at the center of the cell and $\boldsymbol{H}(q)\cdot\boldsymbol{S}$ is the corresponding flux evaluated at the surfaces $\boldsymbol{S}$. That q and $\boldsymbol{H}\cdot\boldsymbol{S}$ reside at distinct spatial positions is a central feature of the finite-volume concept. The total central difference operator $\delta\psi_{ijk}$ equals

$$(\delta_I+\delta_J+\delta_K)\psi_{ijk} = (\psi_{i+\frac{1}{2},j,k}-\psi_{i-\frac{1}{2},j,k}) + (\psi_{i,j+\frac{1}{2},k}-\psi_{i,j-\frac{1}{2},k}) + (\psi_{i,j,k+\frac{1}{2}}-\psi_{i,j,k-\frac{1}{2}})$$

expresses the net gain of flux into the cell and is fundamental to the conservation property and independent of any particular choice of spatial differencing.

Coordinate Geometry

Perhaps the most attractive feature of the finite-volume approach is its readiness to accommodate any type of coordinate system. No global coordinate transformation needs to be specified, in fact the only information about the mesh that we transmit to the method is the three Cartesian coordinates of the eight vertices of every cell in the mesh. With this information it is not even necessary, as it is for a grid-point method, to formulate a local curvilinear coordinate system in order to calculate the metric coefficients of the coordinate transformation. Instead, the equivalent of these terms can be determined strictly by the principles of geometry. For example, altogether ten metric quantities are needed: the three components of each of the three surface areas $\boldsymbol{S}_I$, $\boldsymbol{S}_J$, $\boldsymbol{S}_K$ of a cell together with its volume Ω. If the four vertices

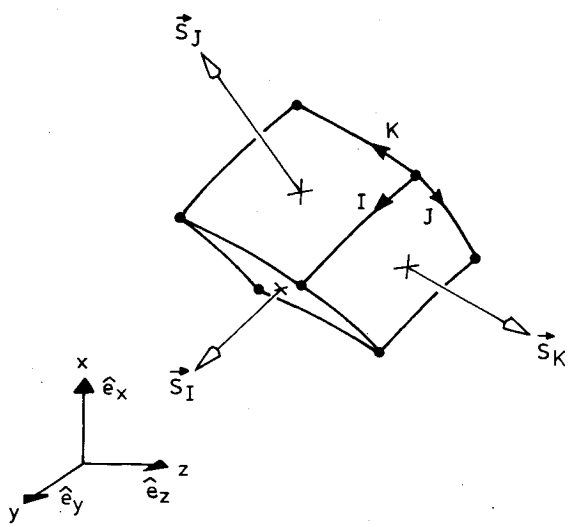

Fig. 1 Hexahedronal mesh cell defined by its eight vertices expressed in Cartesian coordinates.

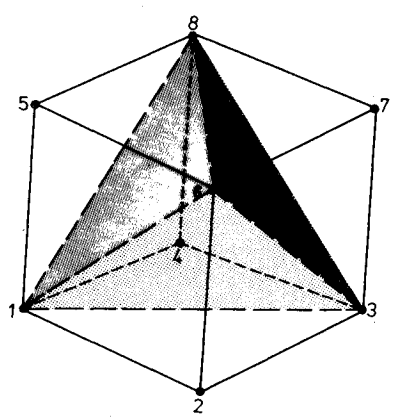

Fig. 2 The volume of a hexahedronal cell is the sum of the five constituent tetrahedra: $T_{1236}+T_{3867}+T_{1685}+T_{1348}+T_{3816}$.

defining a surface are coplanar, its area is given exactly by one half the cross product of its diagonal line segments $S = \frac{1}{2} l_{31} \times l_{42}$: and if they are not coplanar, another exact formula, only slightly more complicated, also exists.[9] The volume Ω is computed in the following way. Without restriction a general hexahedron is composed of five tetrahedra (Fig. 2) each of whose volume is determined exactly by

$$T_{1236} = \frac{1}{6} \begin{vmatrix} x_1 & y_1 & z_1 & 1 \\ x_2 & y_2 & z_2 & 1 \\ x_3 & y_3 & z_3 & 1 \\ x_6 & y_6 & z_6 & 1 \end{vmatrix}$$

where the integer subscripts on T_{1236} refer to the four vertices that define the tetrahedron. The volume of the hexahedron then is the sum of the volumes of these five tetrahedra.

Notice that even if the underlying mesh transformation is singular so that an edge of a cell contracts to a point, a surface collapses to a line or a point, or seven of its eight vertices become coplanar, this geometrical procedure still returns meaningful and accurate values for the areas and volume. The flux quantities therefore can be defined, and since Eq. (2) is balanced in the interior of the cell where no coordinates are used, the numerical solution is well-behaved even in the presence of these mesh singularities. Additionally, this is accomplished automatically without any special programming considerations. The same may not be true for the usual grid-point methods.

Family of Temporally Dissipative Explicit Multistage Schemes

Since q_{ijk} is located in the center of the cell but $H(q)$ must be expressed at its surfaces, some form of local interpolation of the neighboring discrete values q must be devised and a numerical quadrature of the surface integrals performed in order to carry out the discrete solution of Eq. (2). It is the particular type of interpolating function and quadrature that defines the specific spatial difference scheme of the method. In our case we choose the simplest, and perhaps most natural function

$$[H \cdot S]_{ijk} = [H(\mu_I q_{ijk}) \cdot S_I + H(\mu_J q_{ijk}) \cdot S_J + H(\mu_K q_{ijk}) \cdot S_K] \tag{3}$$

where μ is the averaging operator $\mu_I \psi_{ijk} = \frac{1}{2}(\psi_{i+\frac{1}{2},j,k} + \psi_{i-\frac{1}{2},j,k})$. Equation (2) together with Eq. (3) leads to a spatial difference operator completely centered in all three coordinate directions, which of all the second-order accurate schemes probably can be coded with the simplest program structure and which, therefore, offers the largest degree of vectorization. In this paper our attempts to improve the rate at which this centered scheme converges to a steady state is directed exclusively to increasing the dissipation of transients by reducing the time accuracy of the temporal differencing from second to first order.

Gary[10] studied one such centered explicit multistage scheme applied to hyperbolic systems, but it was Jameson[11] who formulated it independently and first brought the concept to our attention. Since then we found that by adding a weighting factor θ to the last step we obtain a family of schemes whose dissipation can be increased by increasing θ. When applied to Eqs. (2) and (3) the family is, with the spatial indices ijk suppressed, the sequence

$$\begin{aligned} \tilde{q}^{(0)} &= q^n \\ \tilde{q}^{(1)} &= q^n - \frac{\Delta t}{2\Omega} [\delta(H \cdot S)^n + \delta(\tilde{H} \cdot S)^{(0)}] \\ &\cdot \quad \cdot \\ &\cdot \quad \cdot \\ \tilde{q}^{(r)} &= q^n - \frac{\Delta t}{\Omega} [(1-\theta)\delta(H \cdot S)^n + \theta\delta(\tilde{H} \cdot S)^{(r-1)}] \\ q^{n+1} &= \tilde{q}^{(r)} \end{aligned} \tag{4}$$

of successive iterates $\tilde{q}^{(r)}$ at each time step Δt and is illustrated schematically for $r = 3$ in Fig. 3. With $\theta > \frac{1}{2}$ it is time accurate to first order and stable for sequence numbers $r \geq 2$ and Courant number $\lambda < 2$. Second-order time accuracy can be attained by using $\theta = \frac{1}{2}$ but then stability is lost for $r = 2, 5, 6, 9, 10\ldots$ irrespective of λ. With $\theta = \frac{1}{2}$ the sequence is identical to Gary's scheme.

It is instructive, and for our purposes it suffices, to analyze the von Neumann stability of this family applied to the linear wave equations $q_t + \sigma q_x = 0$. The amplification factor g then is

$$g = 1 - i\lambda \sin\phi + 4\theta \sum_{m=2}^{r} (-\tfrac{1}{2} i\lambda \sin\phi)^m$$

where now $i^2 = -1$, $\lambda = \sigma\Delta t/\Delta x$ is the Courant number, and $\phi = 2\pi\Delta x/L$ with L the wavelength of the Fourier component. Linear stability is ensured if $|g| \leq 1$ and this is fulfilled if $\lambda \leq$ CFL. The factor g is drawn in the complex plane in Fig. 4 for $r = 3$ and several values of θ together with the corresponding values for CFL. In our application we have no interest in resolving accurately the time evolution, and therefore it is beneficial for the overall convergence to set the parameter θ to a value of 1 or greater in order to increase the damping of the medium-to-long wave transients since it is

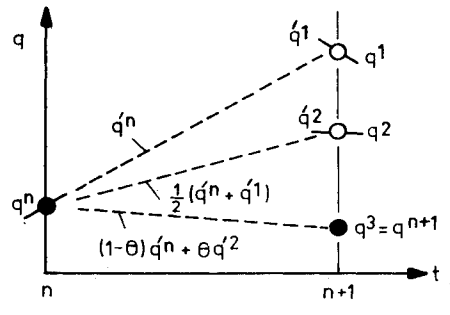

Fig. 3 Schematic illustration of the three-stage scheme. Each new estimate is found by linear projection along a weighted average of the slopes $\dot{q}$ at the original time n (filled circle) and the last previous estimate (open circle).

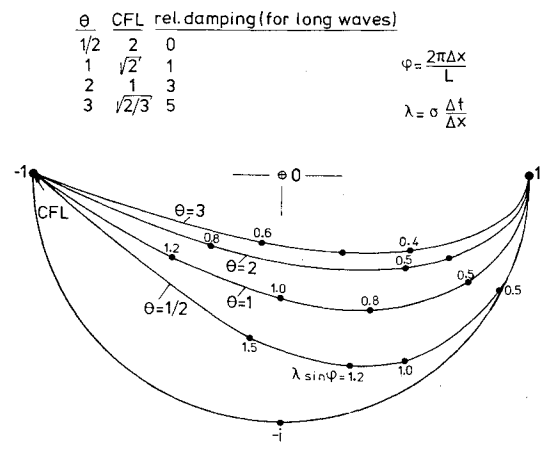

Fig. 4 The amplification factor g of the damped multistage scheme ($r = 3$) drawn in the complex plane for several values of θ.

typically these waves that take the longest time to die out in time-marching methods.

A similar analysis of scheme (4) applied to the linearized Eq. (2) indicates, and it is confirmed by actual numerical tests, that the stability limit on the step size is $\Delta t \leq \min_{ijk}(\Delta t_\ell)$ where

$$\Delta t_\ell = \frac{\Omega_{ijk}}{\frac{1}{2}\kappa(Q_I+Q_J+Q_K)+[\frac{1}{4}\kappa^2(Q_I^2+Q_J^2+Q_K^2)+c^2(S_I^2+S_J^2+S_K^2)]^{1/2}} \tag{5}$$

with

$$Q_I = |V \cdot S_I|, \quad Q_J = |V \cdot S_J|, \quad Q_K = |V \cdot S_K|,$$
$$c^2 = \tfrac{1}{2}\kappa(2h_0 - u^2 - v^2 - w^2)$$

Shuman Filter with Switch

Although scheme (4) effectively damps the medium-to-long wavelength components $L \gg 2\Delta x$, it only slightly dissipates short waves, and this is a drawback of the scheme. It is the admittance of these short waves, for example, in cases where the boundary conditions are not sufficient to control it, that manifest themselves as the uncoupling of the solution at odd and even grid points (notorious to all central difference methods). They are also responsible for the aliasing phenomena since in nonlinear problems they can reappear as distorted long waves. Furthermore, the process of capturing flow discontinuities typically produces short-wave oscillations. The appearance of such unwanted phenomena, however, can be controlled, if not completely eliminated, by a digital filter.[12]

There are a number of ways to approach the design and use of a digital filter, ranging from a heuristic interpretation as some form of artificial viscosity if viewed from a Taylor series expansion to a completely numerical concept based in wave space. It is the latter one that we follow. Supported entirely by the quality of the computed results, the underlying premise in our approach is that only wavelengths longer than some lower limit L_c are important to the accurate steady state, and all shorter waves can be eliminated with impunity by means of a filter. The one we use is the Shuman filter with switch introduced by Harten and Zwas.[13] Let $\tilde{q}^{n+1}$ be the discrete solution $\tilde{q}^{n+1} = Fq^n$ given by scheme (4). Operating on this data set the switched filter S produces the smoothed field

$$q^{n+1} = S\tilde{q}^{n+1} = \tilde{q}_i^{n+1} + \tfrac{1}{4}[\beta_{i+1/2}(\tilde{q}_{i+1} - \tilde{q}_i) - \beta_{i-1/2}(\tilde{q}_i - \tilde{q}_{i-1})]^{n+1}$$

For the complete step we then have a factored operator $q^{n+1} = S \cdot F \cdot q^n$ and the stability of each independently implies the stability of the product.

Accelerated Convergence

It was mentioned earlier that when applied to the Euler equations and a steady state is desired the rate of convergence of a given method depends on how effectively the boundary conditions radiate energy out of the flowfield and how well the scheme itself dissipates transients in the computational domain. However, when explicit time differencing is used, the working of these two mechanisms can be thwarted drastically if the local time step Δt_ℓ varies greatly from one point to another due to the stretching of the mesh. As an example, for a typical case using an O-O mesh the ratio of $\Delta t_{\max}/\Delta t_{\min}$ is almost 1000. Implicit difference methods, of course, are well-suited to handle automatically this type of stiffness caused by the mesh, whereas explicit methods require a form of matrix conditioning of the discrete equations to alleviate at least part of this difficulty, the well-known local time-step technique. Multiplying the spatial terms of Eq. (4) by a conditioning matrix $N = \Delta t_\ell I$ defines a new time path but does not alter the steady-state solution, and the overall effect is to allow very long waves to propagate much more rapidly through the domain.

Boundary Conditions

A particular steady flowfield is determined by the conditions imposed upon it at its boundaries, and usually the stability and accuracy of the discrete conditions are more difficult to analyze than the difference scheme itself. This means that in general the theory of boundary conditions for numerical computations is more empirical. In our case of an O-O mesh conforming to a wing-body combination, boundary conditons are enforced at the six outer surfaces of the computational space (Fig. 5). There are three distinct types: flow into or out of the far field, periodic conditions across coordinate cuts, and conditions on solid walls.

Inflow/Outflow Boundary

With an O-O mesh flow in the far field enters and leaves through the outermost J surface. This is an artificial boundary in the sense that the actual flow in the physical domain is open whereas the computational space must for practical reasons be closed. The numerical conditions, therefore, ideally should allow phenomena generated in the computational domain to pass through the boundary without undergoing significant distortion and without influencing the interior solution. In this way the maximum amount of transient energy escapes from the field, and the time-dependent solution can converge to the steady state. Engquist and Majda[14] present a mathematical theory for the practical application of local absorbing boundary conditions at artificial boundaries.

An alternative to their approach, commonly practiced in meteorological applications, is the concept of a "sponge" layer in which dissipation is introduced in order to damp reflections caused by the boundary. Combining elements of both approaches, we adapt Engquist's first approximation to our problem and then filter the resulting conditions throughout the two outermost J surfaces in an attempt to damp any disturbances caused by the first approximation (see Ref. 15 for the underlying motivation for this step).

The first approximation amounts to specifying the characteristic variables of the corresponding one-dimensional problem which is well-posed and maximal dissipative, but it is easier to grasp the idea if we present our boundary condition in a heuristic development based on the characteristic variables instead of the formal theory. The presentation for

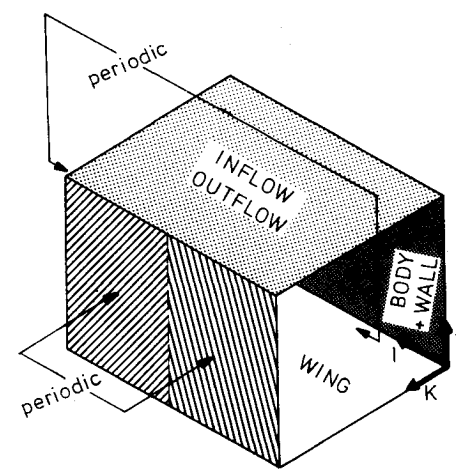

Fig. 5 Types of boundary conditions on the six outer surfaces of the computational space *IJK* resulting from the O-O grid mapping.

our 4×4 system mirrors the one given by Gottlieb and Gustafsson[16] for the 3×3 system.

At a point P on the outer boundary position local rectangular coordinates X, Y, Z with X normal to the surface and positive into the domain, the other two being tangent to the surface. In this system the quasilinear equations equivalent to Eq. (1) but locally linearized about a known state q are

$$\tilde{q}_t + A\tilde{q}_X = -B\tilde{q}_Y - C\tilde{q}_Z$$

where

$$\tilde{q} = \begin{bmatrix} \tilde{U} \\ \tilde{V} \\ \tilde{W} \\ \tilde{\rho} \end{bmatrix} \text{ and } A = \begin{bmatrix} (1-\kappa)U & -\kappa V & -\kappa W & c^2/\rho \\ 0 & U & 0 & 0 \\ 0 & 0 & U & 0 \\ \rho & 0 & 0 & U \end{bmatrix}$$

We seek the characteristic variables of the corresponding one-dimensional problem

$$\tilde{q}_t + A\tilde{q}_X = 0 \tag{6}$$

which means that we focus on a particular set of characteristic planes, those whose normals point along X and whose slopes in time are the eigenvalues λ of A. Solving det $(A-\lambda I)=0$ we find

$$\lambda_1 = U, \quad \lambda_2 = U, \quad \lambda_3 = U - a_-, \quad \text{and} \quad \lambda_4 = U - a_+$$

where $a_\pm = \frac{1}{2}\kappa U \pm (\frac{1}{4}\kappa^2 U^2 + c^2)^{1/2}$. The left and right eigenvectors associated with these four eigenvalues make up the rows and columns of the transformation matrices T^{-1} and T, respectively, that diagonalize Eq. (6)

$$\phi_t + \Lambda\phi_x = 0$$

where

$$\phi = T^{-1}\tilde{q} \qquad \Lambda = T^{-1}AT = \mathrm{diag}\{\lambda_1\lambda_2\lambda_3\lambda_4\}$$

$$T^{-1} = \begin{bmatrix} 0 & 1 & 0 & 0 \\ 0 & 0 & 1 & 0 \\ -\rho a_- & -\kappa\rho V & -\kappa\rho W & c^2 \\ \rho a_+ & \kappa\rho V & \kappa\rho W & -c^2 \end{bmatrix}$$

$$T = \begin{bmatrix} 0 & 0 & \dfrac{1}{\rho(a_+ - a_-)} & \dfrac{1}{\rho(a_+ - a_-)} \\ 1 & 0 & 0 & 0 \\ 0 & 1 & 0 & 0 \\ \dfrac{\kappa\rho V}{c^2} & \dfrac{\kappa\rho W}{c^2} & \dfrac{a_+}{c^2(a_+ - a_-)} & \dfrac{a_-}{c^2(a_+ - a_-)} \end{bmatrix}$$

For the one-dimensional case it is well-known that the number of conditions to be imposed at P should equal the number of characteristic directions which enter the computational domain. Four typical cases are depicted in Fig. 6. With subsonic inflow our implementation is to set the three ingoing characteristic variables $\phi^{(1)}$, $\phi^{(2)}$, and $\phi^{(3)}$ to their freestream values, linearly extrapolate the fourth $\phi^{(4)}$ from the computational field, and then solve for the original unknowns $q = T\phi$. At outflow it is $\phi^{(3)}$ that is given the values of undisturbed flow, and $\phi^{(1)}$, $\phi^{(2)}$, and $\phi^{(4)}$ are extrapolated. These variables $\tilde{q}$ determined at the boundary together with their nearest neighbors in the J direction are then filtered.

Coordinate Cuts

Conditions on these boundaries are the least troublesome since at a cut the physical space folds onto itself and the condition on the flow at the computational boundary is periodicity. We remark that in the O-O topology these boundaries occur conveniently at the trailing edge and tip of the wing (Fig. 5).

Solid Walls

For inviscid flow the imposition of the boundary condition on the surface of the aerodynamic vehicles of interest in our work possesses two different but related aspects. The first is the usual one that no flow is allowed through a solid wall, and the second is the so-called Kutta condition which dictates how vorticity, and therefore lift and drag, is generated at the surface in an initially irrotational flow.

Zero Flux Transport

The physical condition of zero transport $\boldsymbol{V}\cdot\boldsymbol{n}=0$ applies to two surfaces, the wing $J=1$ and the fuselage which merges together with the wall of symmetry $K=1$ (see Fig. 5). Since the computational cells are aligned to both these surfaces, the physical condition reduces the dependence of $\boldsymbol{H}(q)_{\mathrm{veh}}$ to $\boldsymbol{H}(p)_{\mathrm{veh}}$, and we are forced to determine a value for p on the vehicle surface by numerical means, usually by differencing some auxiliary equation in order to relate values in the field to those on the surface. Our procedure to obtain an estimate of p_{veh} from the interior solution has been described before in the general case.[17] It is valid at both the wing and the body-plus-wall surfaces, and we summarize it briefly. The basis of our auxiliary relation for p_{veh} begins with the streamline differentiation of the physical condition $(\partial/\partial t + \boldsymbol{V}\mathrm{grad})(\boldsymbol{V}\cdot\boldsymbol{n}) \equiv 0$ where $\boldsymbol{n}$ is the unit vector normal to either the wing or fuselage. This expression when combined with the inner product of the quasilinear momentum equation and $\boldsymbol{n}$ and rearranged, becomes, for a stationary vehicle,

$$\rho\boldsymbol{V}\cdot(\boldsymbol{V}\cdot\mathrm{grad})\boldsymbol{n} = \boldsymbol{n}\cdot\mathrm{grad}p \tag{7}$$

$$\mathrm{grad} = n_I\frac{\partial}{\partial x_I} + n_J\frac{\partial}{\partial x_J} + n_K\frac{\partial}{\partial x_K}, \quad \boldsymbol{n} = \begin{cases} n_J \\ \text{or} \\ n_K \end{cases}$$

and relates ρ, $\boldsymbol{V}$, and the geometry of the surface to the normal derivative of p. When it is differenced to formally first-order accuracy the pressure on the surface is deduced from the interior values.

Kutta Condition

Because a velocity potential satisfies curl $\boldsymbol{V}=0$ identically, the exact solution of potential flow past a wing as well as any

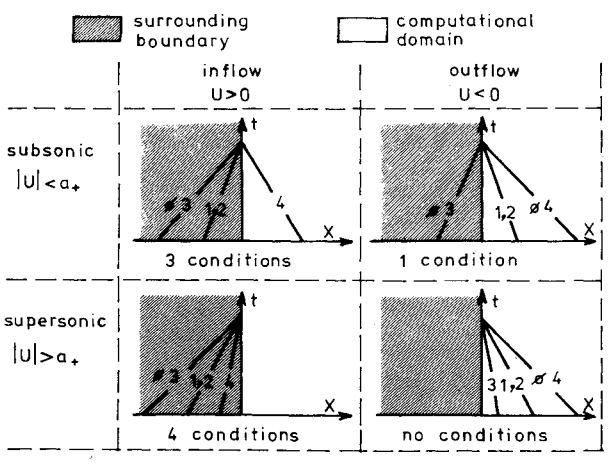

Fig. 6 The number of boundary conditions at inflow and outflow based on the ingoing characteristic variables ϕ^m, $m=1\ldots4$.

finite-difference approximation to it cannot admit distributed vorticity in the field. Numerical methods based on a potential therefore introduce a jump in potential across a cut in the field in order to represent the vorticity generated by the wing so that nonzero values for lift and induced drag can be realized, a procedure generally termed the Kutta condition. During a workshop[1] on transonic flow those methods which solved the Euler equations for flow past an airfoil section but which did not implement any explicit procedure to introduce vorticity still obtained accurate solutions with the correct lift. How this could be, it was argued, is that the Euler equations unlike the potential equation admit vorticity and vortex sheets as genuine and weak solutions, respectively, so that they can be "captured" in the same sense that shock waves can be captured, and a Kutta condition need not be enforced explicitly. Here we report further that in our computed examples of three-dimensional flow past a finite wing we also do not impose a Kutta condition explicitly but we still obtain solutions with the correct lift.

In an attempt to explain this observation we offer the following hypothesis that suggests a mechanism in the Euler equations which automatically places the separating stream at the sharp trailing edge of the wing. In steady flow a fluid surface meeting the smooth leading edge of a wing bifurcates into two streams that ultimately merge again at the sharp trailing edge. It is precisely this confluence of previously separated fluid that can generate vorticity even in the absence of viscosity. The process is fundamentally unsteady and we examine it in more detail. Begin with a wing, initially at rest in a nonviscous fluid which then starts to accelerate. In the first instant a qualitative picture of the streamlines around any cross section of the wing is given in Fig. 7a. The streamlines are of potential type, attachment at A, detachment at B, and flow around the trailing edge S. The next phase of the process occurs near S, and we can examine the flow there in isolation for a moment. On the one hand (Fig. 7b), if it obeys a potential equation, the flow exhibits a very high velocity and low pressure at S (plus and minus infinity, respectively, in the limit) but has sufficient kinetic energy to turn and follow the surface up to stagnation at B. However, on the other hand, if it obeys the Euler equations (Fig. 7c), it will attempt to accelerate through an expansion fan around S, but now the theoretical limits of these equations are finite velocity and zero pressure, i.e., the flow can expand down to vacuum only. In the approach to this limit the flow is surely unsteady and supersonic, and in analogy to flow in a shock tube or explosion we should expect the appearance of an expansion fan, a contact (tangential) discontinuity, and a shock wave (Fig. 7c). It is difficult to predict precisely how in the confluence of two different streams these various features interact, but it seems likely that the shock would drain enough kinetic energy from the flow to retard it and draw fluid from B toward S. If it does, the effect is to strengthen the tangential discontinuity (Fig. 7d) into a surface of separation with unequal velocities on each side. This surface, a vortex sheet, begins to roll up under the action of its own induced velocity (Fig. 7e), it turns into a vortex along the entire trailing edge of the wing and is shed due to the convection of the surrounding stream (Fig. 7f).

The sense of the shed vorticity acts to impede the velocity around the trailing edge so that B is drawn toward S in a stable and self-correcting process until fluid no longer expands around the trailing edge, but flows off tangentially at both sides with velocities that may differ only in direction (steady flow) or magnitude as well (unsteady flow). Simultaneously, fluid driven from the high-pressure surface of the wing and around the tips to the low-pressure surface generates two trailing vortices that connect the tips of the wing and the ends of the shed vortex, and forms the familiar horseshoe vortex. It can be reasoned furthermore that this generation of vorticity does not contradict Kelvin's theorem.[18]

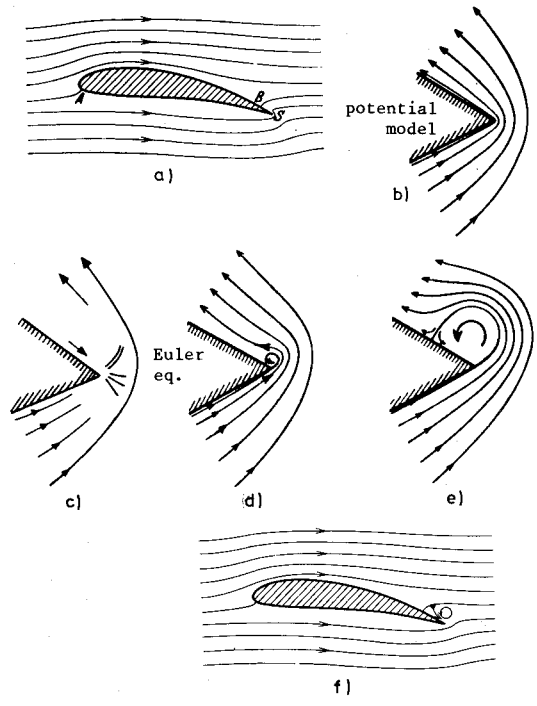

Fig. 7 Phenomenological sketch of streamlines of inviscid potential and rotational flow around a wing during its first instants of acceleration from rest: a) flow around sharp trailing edge S; b) potential model, flow around S allowed; c) Euler equations, flow expands to vacuum in the limit; d) separates with a tangential discontinuity; e) rolls up into a vortex; and f) is shed drawing B to S.

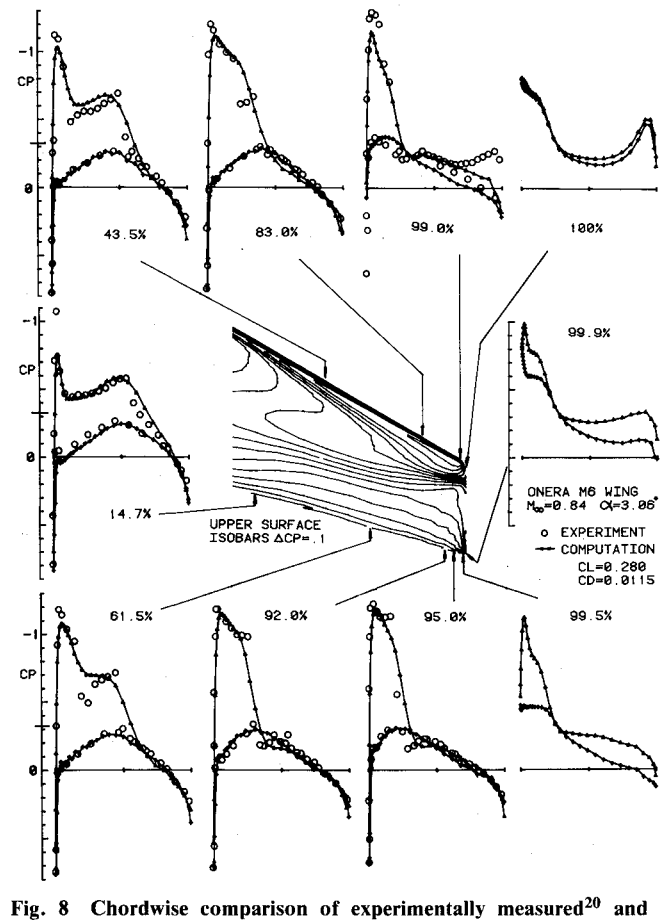

Fig. 8 Chordwise comparison of experimentally measured[20] and computed distributions of pressure coefficient C_p together with the computed isobar contours on the upper surface of the ONERA M6 wing; $M_\infty = 0.84$ and $\alpha = 3.06$ deg.

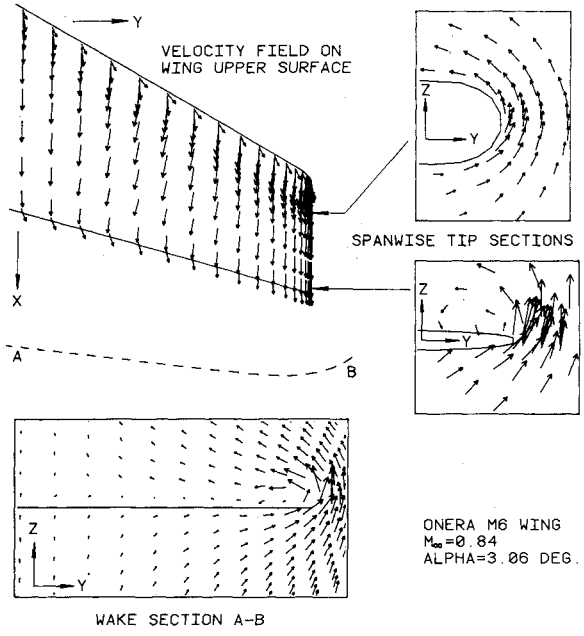

Fig. 9 Selected views of the computed velocity field around and in the wake of the ONERA M6 wing; $M_\infty = 0.84$ and $\alpha = 3.06$ deg.

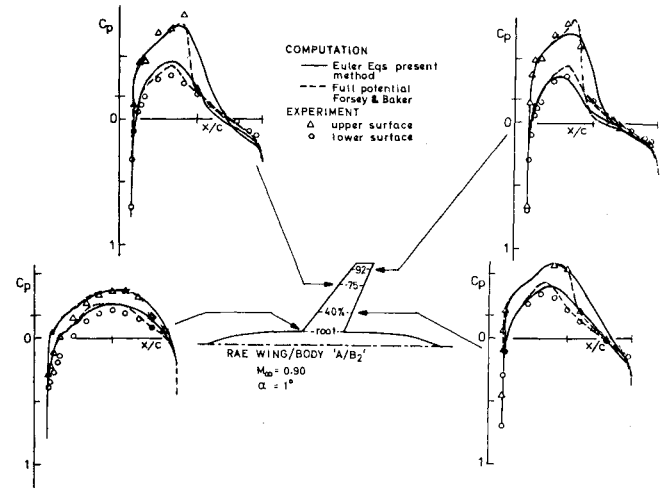

Fig. 10 Chordwise comparison of computed and measured[20] pressure coefficients C_p on the RAE A/B$_2$ wing-body combination; $M_\infty = 0.90$ and $\alpha = 1$ deg.

We must emphasize that it is the salient trailing edge that controls the entire process just described. If the surface is smooth (more precisely, if the local radius of curvature is sufficiently large), the preceding mechanism will not be enacted, and the flow will not separate there. This has been confirmed in some numerical experiments of flow around a smooth body. Without any Kutta condition our solution of the Euler equations had zero lift and agreed closely with a corresponding potential solution. The implication is that an explicit Kutta condition is necessary to obtain a solution with lift for flow around a smooth body, but is not necessary if the body has a salient edge.[19] There are several ways to implement a Kutta condition directly at any chosen point on a body, and one is discussed in Ref. 19. The lift obtained in the solution varies directly with location of that point, and to obtain the realistic value of lift on a smooth body, the position for the Kutta condition must be given by viscous theory.

Computed Examples

Computed results of two example subsonic-freestream flows, one past a wing alone and the other a wing-body combination, are presented to demonstrate the overall range of applicability of our method and the nature of the solutions obtained. All of our results were computed on an O-O type grid with the parameters of scheme (4) set to $\theta = ½$ and $r = 3$, and no explicit Kutta condition was implemented. The method also treats very effectively the flow around a sharp-edge delta wing. In Ref. 19 we present solutions that realistically represent the vortex shed from the leading edge of the delta wing in supersonic as well as subsonic flight.

Wing Alone—ONERA M6

The mesh presented in Fig. 12 of Ref. 6 containing $64 \times 14 \times 20$ cells offers sufficient resolution at the tip in order to obtain the details of the flow there, and our solution computed upon it for the flow $M_\infty = 0.84$ and $\alpha = 3.06$ deg past the ONERA M6 wing is displayed in Figs. 8 and 9. Shown in Fig. 8 are contours of constant C_p values on the upper surface along with those chordwise sectional plots that fall closest to the seven sections that have been measured experimentally.[20] Bearing in mind that the field contains fewer than 18,000 cells we judge the comparison to be quite good. The 99.0% section, however, is most interesting. On the rear upper surface of the chord the measurements reveal a substantial re-expansion of the flow that is matched in part by a similar trend in the computation. (We should add that the exact geometry of the tip used for the wind-tunnel test is not specified.) This trend continues in the following computational sections so that at the 100% station the location and strength of the computed re-expansion is very close to the one observed at 99%. That there is little difference between the upper and lower surface also agrees with aerodynamic theory and the absence of a high-pressure region is due to the rounded leading corner of the tip. The flow expands to supersonic speed right before the trailing corner of the tip where there is an abrupt compression, a sure telltale of separation. This is ascertained even more concretely from the velocity fields given in Fig. 9. Here we see that in the upstream part of the tip region the flow follows the tip surface in perfect character with an irrotational fluid, whereas further downstream it separates from the surface creating a rotational flow above the upper surface of the wing. This tip separation phenomenon, we believe, provides the most convincing evidence to date for the existence of a purely inviscid mechanism for separation in the Euler equations.

Also shown in Fig. 9 is a velocity-vector plot of the transverse flow in a wake section that clearly displays the position of the tip vortex and the slightly smeared vortex sheet emanating from the trailing edge. For a reference length, the trailing edge is projected onto this section and indicated by the single line. It is interesting to point out that the center of the vortex sheet seems to be positioned slightly above the wing plane and, furthermore, that the center of the tip vortex is displaced inboard. These are typical effects, often observed in experiments and in the results of vortex-lattice methods with wake-vortex relaxation.

Wing-Body—RAE A/B$_2$

For flow conditions $M_\infty = 0.90$, $\alpha = 1$ deg around the RAE wing-body combination A/B$_2$ Fig. 10 presents our computed coefficient of pressure C_p at several selected spanwise locations and compares them with results from the solution of the full potential[21,22] equation computed on an O-H grid of $160 \times 20 \times 24$ nodal points together with experimentally measured values.[20] Considering that the number of grid points used for the potential solution is over six times the number we used ($64 \times 14 \times 14$), we deem the overall agreement good. Our suction peaks and shock waves at the two inboard sections are broader than the other results, due no doubt to our larger grid spacing and the lack of sharpness in the Shuman filter. At the root sections both computations agree reasonably well with each other (except toward the trailing

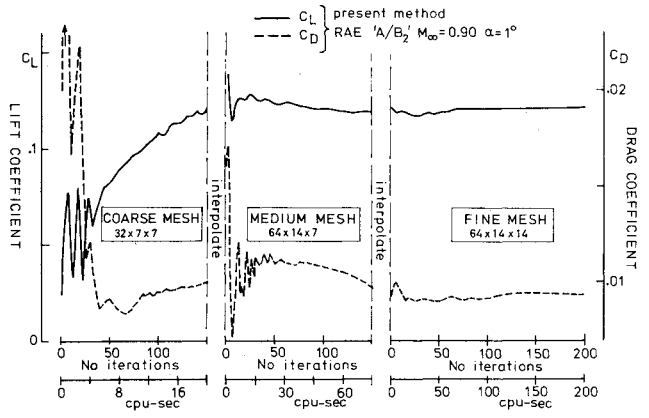

Fig. 11 Time evolution of the computed lift and drag coefficients C_L and C_D using successive grid refinement. Computer execution time for CYBER 203 vector processor. RAE A/B$_2$ $M_\infty = 0.90$ and $\alpha = 1$ deg.

edge) but differ from the measured values. At each of the other three sections there is a lack of agreement in the vicinity of the suction peaks on the lower surface. However, the most substantial difference is that the shocks occur further aft in the Euler solution than in either the potential solution or the measurements, primarily due, we believe, to the coarseness of our mesh for this wing-body combination.

Convergence to Steady State

In each of the computed examples the freestream flow is used as the initial conditions for the computation which begins impulsively on the first (coarse) of three successively refined O-O grids. After 150 iterations this coarse field is interpolated to the next refined (medium) mesh, marched another 150 steps to when it is interpolated again to the last (fine) grid, and advanced the final 100-200 iterations. The effectiveness of this strategy of successive grid refinement is shown in the plot (Fig. 11) of the time evolution of the lift and drag coefficients C_L and C_D. Because of the large cell size of the coarse mesh signals can travel rapidly through the field and escape through the outer boundary relatively quickly. On the first 50 steps we see large-amplitude adjustments in C_L and C_D, followed by damped progression toward steady values. Notice that even after the first iteration a nonzero lift is realized, an indication of how rapidly the tangential discontinuity develops at the trailing edge even without an explicit Kutta condition. The execution time of the optimized scalar code on the CYBER 203 vector processor is 1 CPU-second/step in the fine mesh. The entire 3-level computation in Fig. 11 expended a total of about 310 CPU-second on the CYBER 203. That this method can start impulsively and advance with the local time step for the entire computation is an indication of its robustness. The algorithm is currently being vector coded with hopes for a 60-70% reduction in execution time.

Concluding Remarks

The goal in the development of our numerical procedure in application of flow around wing-body combinations has been to increase its convergence rate. An explicit temporally dissipative difference scheme followed by a factored filter operator together with nonreflecting boundary conditions are means to this end and deserve further development. However, we would be remiss if, when devising numerical techniques to meet this goal, we overlooked the computational efficiency offered by the vector-processing computers. For it is not the convergence rate per se, but rather the accuracy obtained per unit computational cost that sits in final judgement of the utility of a given method. Because of the total absence of matrix procedures, explicit schemes and multiplicative operators like filters offer a great deal of freedom to exploit the fruits of vector processing.

Acknowledgments

Our thanks go to a number of people and institutions who have contributed to this work during the past two years: A. Jameson and W. Schmidt for sharing with us their ideas about centered schemes and multiplicative filtering, B. Gustafsson for a number of stimulating discussions about convergence and boundary conditions, Control Data Corporation for introducing us to the world of vector processing, Dornier GmbH for its hospitality when I visited in August 1980, and, finally, the Air Materiel Department of the Swedish Defence Materiel Administration who sponsored the entire effort.

References

[1]Rizzi, A. W. and Viviand, H., eds., "Numerical Methods for the Computation of Inviscid Transonic Flow with Shocks," *a GAMM Workshop, Notes on Numerical Fluid Mechanics,* Vol. 3, Vieweg Verlag, 1981.

[2]Thompkins, W. T. and Oliver, D. A., "Three-Dimensional Flow Calculation for a Transonic Compressor Rotor," *AGARD Conference Proceedings,* 195, 1976.

[3]Denton, J. D. and Singh, V. K., "Time Marching Methods for Turbomachinery Flow Calculations," VKI, Lecture Series 1979-7.

[4]Brochet, J., "Numerical Computation of 3-D Transonic Internal Flows," *Recherche Aerospatiale,* No. 5, 1980, pp. 301-315.

[5]Rizzi, A. and Eriksson, L. E., "Transfinite Mesh Generation and Damped Euler Equation Algorithm for Transonic Flow Around Wing-Body Configurations," AIAA Paper 81-0999, June 1981.

[6]Eriksson, L. E., "Generation of Boundary-Conforming Grids Around Wing-Body Configurations Using Transfinite Interpolation," *AIAA Journal,* 1982.

[7]Viviand, H., "Pseudo-Unsteady Methods for Transonic Flow Computations," *Proceedings of the 7th International Conference on Numerical Methods in Fluid Dynamics,* edited by W. Reynolds, *Lecture Notes in Physics,* Springer Verlag, 1981.

[8]Rizzi, A. W., "Computation of Rotational Transonic Flow," *Numerical Methods for the Computation of Inviscid Transonic Flow with Shocks, a GAMM Workshop,* edited by A. W. Rizzi and H. Viviand, *Notes on Numerical Fluid Mechanics,* Vieweg Verlag, 1981.

[9]Schmidt, W., private communication, Dornier GmbH, 1981.

[10]Gary, J., "On Certain Finite Difference Schemes for Hyperbolic Systems," *Mathematics of Computations,* Vol. 18, 1964, pp. 1-18.

[11]Jameson, A., Schmidt, W., and Turkel, E., "Numerical Solutions of the Euler Equations by Finite Volume Methods Using Runge-Kutta Time Stepping," AIAA Paper 81-1259, June 1981.

[12]Hamming, R. W., *Digital Filters,* Prentice-Hall, 1977.

[13]Harten, A. and Zwas, G., "Switched Numerical Shuman Filters for Shock Calculations," *Journal of Engineering Mathematics,* Vol. 6, April 1972, pp. 207-216.

[14]Engquist, B. and Majda, A., "Absorbing Boundary Conditions for the Numerical Simulation of Waves," *Mathematics of Computations,* Vol. 31, July 1977, pp. 629-651.

[15]Israeli, M. and Orszag, S. A., "Approximation of Radiation Boundary Conditions," *Journal of Computational Physics,* Vol. 41, 1981, pp. 115-135.

[16]Gottlieb, D. and Gustafsson, B., "On the Navier-Stokes Equations with Constant Total Temperature," *Studies in Applied Mathematics,* Vol. 55, 1976, pp. 167-185.

[17]Rizzi, A. W., "Numerical Implementation of Solid-Body Boundary Conditions for the Euler Equations," *ZAMM,* Vol. 58, 1978, pp. T301-T304.

[18]Prandtl, L. and Tietjens, 0., *Fundamentals of Hydro- and Aeromechanics,* Dover, 1957, p. 193.

[19]Eriksson, L. E. and Rizzi, A., "Computation of Vortex Flow Around Wings Using the Euler Equations," *Proceedings of the IVth GAMM Conference on Numerical Methods in Fluid Mechanics,* edited by H. Viviand, Vieweg Verlag, Paris, Oct. 1981.

[20]*Experimental Data Base for Computer Program Assessment,* AGARD-AR-138, May 1979.

[21]Forsey, C. and Carr, M., "The Calculation of Transonic Flow over Three-Dimensional Swept Wings using the Exact Potential Equation," DGLR Symposium Transonic Configurations, Bad Harzburg, June 1978.

[22]Baker, T. and Forsey, C., "A Fast Algorithm for the Calculation of Transonic Flow over Wing/Body Combinations," AIAA Paper 81-1015, June 1981.